Performance optimization of supercritical CO2 gas heater in a biomass-CO2 power generation system

X. Zhang, Y.T. Ge*

School of the Built Environment and Architecture

London South Bank University, 103 Borough Road, London , SE1 0AA, UK

ABSTRACT

A comprehensive Computational Fluid Dynamics (CFD) simulation model was developed in the current research to simulate a shell-and-tube supercritical CO_2 gas heater used in a biomass-CO_2 power generation system. The model was based on the actual design of the heat exchanger and relevant operational parameters. The simulation model was validated using manufacturer operational data and empirical correlations before being utilized to evaluate the performance of the heat exchanger and its related system under various operating conditions and heat exchanger designs. The results of the simulation demonstrate that the heating capacity of the heat exchanger can be increased differently by increasing the flue gas temperature, flue gas mass flow rate, and CO_2 mass flow rate. Furthermore, there is an optimal CO_2 pressure ratio that can improve the system's thermal efficiency. Decreasing the distance between hot fluid pipe inlet and cold fluid outlet ports, as well as hot fluid pipe outlet and cold fluid inlet ports, can effectively enhance the heating capacity of the shell-and-tube heat exchanger (STHX) and its associated system. Based on the CFD simulation outcomes, recommendations for enhancing the heat exchanger designs and system controls have been identified.

Keywords: shell-and-tube CO_2 supercritical gas heater, biomass-CO_2 power generation system, Computational Fluid Dynamics (CFD) modelling, performance analysis and optimisation.

* Corresponding author.

E-mail address: yunting.ge@lsbu.ac.uk (Y.T. Ge)

Nomenclature

A_s	bundle crossflow area (m^2)
c_p	specific heat at constant pressure ($J\ kg^{-1}K^{-1}$)
d	diameter (m)
D_e	equivalent diameter (m)
D_s	shell side diameter (m)
f	friction factor
G_s	mass flux ($kg\ m^{-2}\ s^{-1}$)
h	heat transfer coefficient ($W\ m^{-2}\ K^{-1}$)
H	enthalpy ($J\ kg^{-1}$)
J_c	segmental baffle window correction factor
J_l	correction factor for baffle leakage effects
J_b	correction factor for bundle bypass effects
J_s	correction factor for baffle spacing
J_r	correction factor for laminar flow
K	thermal conductivity ($W\ m^{-2}\ K^{-1}$)
L	length of tubes (m)
$\dot{m}$	mass flow rate ($kg\ s^{-1}$)
N	number of tubes
Nu	Nusselt number
P	pressure (Pa)
Pr	Prandtl number
ΔP_c	pressure drop in the cross flow section (Pa)
ΔP_w	pressure drop in the window (Pa)
ΔP_e	pressure drop in the entrance and exit sections (Pa)
Q	heat transfer rate (W)
Re	Reynolds number
STHXA	shell-and-tube heat exchanger A
STHXB	shell-and-tube heat exchanger B
T	temperature (K)
U	overall heat transfer coefficient ($W\ m^{-2}\ K^{-1}$)
W	work input/output (W)

x, y, z position coordinates

Greek symbols

μ molecular viscosity (Pas)

μ_t turbulent molecular viscosity (Pas)

σ_k turbulent Prandtl number for energy dissipation rate

σ_ε turbulent Prandtl number for kinetic energy

ν kinematic molecular viscosity ($m^2\ s^{-1}$)

ρ density ($kg\ m^{-3}$)

u_i, u_j velocity components in ith and jth direction ($m\ s^{-1}$)

k turbulent kinetic energy ($m^2\ s^{-2}$)

ε effectiveness

η thermal efficiency

Subscripts

av average

b baffle

i inner

in inlet

m mean

o outer

out outlet

s shell side

sm mean on shell side

t tube side

tm mean on tube side

1. Introduction

Although fossil fuels currently dominate energy resources for power generation and heating worldwide, their limited availability and negative environmental impacts make it imperative to utilize renewable energy or industrial waste heat in energy conversion systems. Biomass, a non-fossilized and biodegradable organic material generated from plants, animals, and microorganisms, has become a

global leader in the development of low-carbon electricity and heating. However, currently biomass provides less than 15% of the world's energy supply [1], indicating room for improvement in energy utilization efficiency. When a biomass boiler is used solely for hot water production, the boiler's exergy efficiency is very low. To address this, the high flue gas temperature of biomass combustion (up to 800°C) can first be used for power generation with an appropriate thermodynamic power cycle and then for hot water production. This approach can significantly reduce irreversible energy losses and improve energy utilization and exergy efficiency. A CO_2 transcritical (T-CO_2) or supercritical CO_2 (S-CO_2) Brayton cycle is a better option for power generation using the high-temperature heat source of biomass flue gas, considering the compactness and higher performance efficiency of its associated system [2-4].

The supercritical CO_2 gas heater is a crucial component in the T-CO_2 or S-CO_2 power generation system, as it significantly impacts system performance. Shell-and-tube heat exchangers have enjoyed widespread use in industries and energy systems, such as refrigeration and heat pump applications, owing to their straightforward designs, compactness, ease of maintenance, and relatively high performance. Given the high temperatures and pressures involved in the heat transfer fluids, a shell-and-tube heat exchanger is a suitable CO_2 gas heater for use in the biomass-CO_2 power generation system [5]. In this system, CO_2 flows through the tube side, while the flue gas passes along the shell side. However, the operational efficiency of the CO_2 gas heater must be further improved, necessitating highly efficient thermal hydraulic behaviours and optimal structural designs concerning the positioning of the flue gas inlet and outlet ports, tube diameters, positions and numbers, and baffle cut ratios, numbers, and position arrangements, among other factors. Consequently, several experiments have been conducted to investigate the fundamental calculations of heat transfer coefficients and pressure drops of shell-and-tube heat exchangers under various design and operating conditions [6-7]. A study by Kim and Aicher [8] was conducted to investigate the heat transfer characteristics of a shell-and-tube heat exchanger, with a focus on varying its structural parameters. The research revealed that the impact of tube pitch could be disregarded. Furthermore, for a heat exchanger with a shorter tube length, the shell-side fluid heat transfer coefficient in the tube nozzle region was found to be considerably higher than that in the tube parallel regions situated in the vicinity. The study also demonstrated that, in the case of a shell-and-tube heat exchanger with staggered tube arrangement, the local shell-side heat

transfer coefficient in the inlet nozzle was considerably greater than that observed in other flow regions [9]. Furthermore, He et al. [10] conducted a study and discovered that a shell and tube heat exchanger utilizing elliptic tubes exhibited a 14.7-16.4% higher heat transfer rate compared to the heat exchanger employing circular tubes. However, the flow characteristics of the shell side are intricate and arduous to measure owing to the presence of baffles. The use of baffles in shell-and-tube heat exchangers is to direct the fluid flow of the shell side, prevent tube bundles from sagging, and avoid the effects of vibration. The conventional segmental baffle arrangement often leads to dead zones, resulting in a lower heat transfer rate [11]. To mitigate this negative impact, it has been demonstrated that by increasing the number of baffles, the dead zones could be effectively eliminated [12], although this may result in higher pressure drops on the shell side. Halle et al. [13] performed an investigation on the shell-side fluid pressure drops of shell-and-tube heat exchangers with different baffle configurations. Their results indicated that closer baffle spacing resulted in higher fluid flow velocity and improved heat transfer, but at the expense of higher pressure drop. Similarly, the findings of Sparrow and Reifschneider [14] indicated that a greater pressure drop resulted in higher pumping power. Moreover, the cut ratio of the baffle was found to increase the heat transfer but also caused a concomitant increase in pressure drop [15]. A helically baffled shell-and-tube heat exchanger has been proposed as a viable alternative to conventional segmental baffle arrangements, owing to its potential to overcome their limitations. This has been demonstrated through both experimental and numerical investigations [16-18]. It is understood that these experimental investigations were mostly on the performance effects of varied heat exchanger structural designs. However, for the biomass-CO_2 gas heater studied in this paper, the effects of varied operating conditions and thermophysical properties of high temperature supercritical CO_2 fluid flow on the heat exchanger performance are also important. The thermal match between shell-side flue gas and tube-side CO_2 flows can contribute significantly to the reduction of heat transfer irreversibility and thus improvement of the heat exchanger performance [19].

Theoretically, in order to estimate the performance of shell-and-tube heat exchanger, two widely recognized methods, by Bell-Delaware [20] and Kern [21] have been utilized to evaluate fluid heat transfer coefficients and pressure drops on the shell side fluid flow. However, the Bell-Delaware method is considered to be more precise in predicting the heat transfer performance of shell side fluid flow, as

it takes into account the effects of leakage and bypass streams on shell side fluid flow. Based on the correlations and equations derived from the Bell-Delaware method, Gaddis and Gnielinski [22] have conducted an assessment and update of shell side pressure drop calculations. Alternatively, Jayachandriah and Vinay [23] have employed Kern method to design shell-and-tube heat exchangers with different baffle arrangements. Furthermore, Kern and Bell-Delaware methods have been utilized for heat exchanger model validations [24-25]. However, the methods mentioned above cannot be used for effectively design optimisation of the heat exchangers, owing to the complex structures involved. In contrast, the use of a well-developed computational fluid dynamics (CFD) model can facilitate the optimization of heat exchangers with different designs and operating conditions. This modelling strategy allows for a more thorough investigation of fluid flow dynamics and heat transfer behaviour prior to any further actions. In comparison to expensive experimental investigations and design, a validated CFD model is a more cost-effective and valuable means of achieving optimal design for heat exchangers. According to the studies conducted by Lei et al. [26-27], a microtube heat exchanger and a printed circuit heat exchanger (PCHE) were chosen as a CO_2 gas heater and a recuperator in supercritical CO_2 Brayton cycles, respectively. CFD simulations were performed to assess their performance. Furthermore, the PCHE with zigzag channel was evaluated numerically for the S-CO_2 power cycles [28]. The results showed that the zigzag channel utilizing supercritical CO_2 as the working fluid, held promise for heat transfer enhancements and heat exchanger designs in high-temperature and high-pressure systems. Nevertheless, the shell-and-tube heat exchangers remain one of the most promising gas heaters for use in S-CO_2 Brayton cycles. They are designed and manufactured with extreme flexibility and stability, enabling them to withstand both high and low temperatures and pressures, and are they also suitable for applications that require a large heat transfer area. Further studies on this type of heat exchanger and its integration with power generation systems are warranted. The proper operation of supercritical/transcritical CO_2 Brayton cycle requires efficient heating of the working fluid, and accurate modelling and simulation can help optimize the design of the gas heater for maximum efficiency and performance. By utilizing precise CFD models to optimise the designs of CO_2 gas heaters, researchers cany save significantly the development time and expense for S-CO_2 power cycles and systems while simultaneously boost their efficiency and dependability.

According to the literature reviewed, conventional shell-and-tube heat exchangers have been studied both experimentally and theoretically to evaluate their performance and optimize their design. The investigated heat exchangers have primarily been utilized in industrial processes, refrigeration, and heat pump systems, with working fluids including steam, water, and various types of refrigerants. In addition, although the shell-and-tube heat exchangers have been recommended in supercritical or transcritical CO_2 Brayton cycles or systems, they were generally investigated as CO_2 gas coolers or recuperators instead of supercritical CO_2 gas heaters [29-32]. Furthermore, conventional shell-and-tube heat exchangers have often been studied in isolation from their corresponding systems, leading to uncertainties regarding their effects on system performance under varying designs and operational conditions. The overall system efficiency of a CO_2 transcritical or supercritical power cycle is greatly affected by the design and performance of the CO_2 gas heater [33]. To the best of the authors' knowledge, there have been limited investigations on the design and operation of a practical high-temperature biomass flue gas heated supercritical CO_2 shell-and-tube gas heater, as well as their influence on the performance of the associated system by the utilization of CFD model. As a result, this study aims to develop and validate a comprehensive computational fluid dynamics (CFD) model of the CO_2 supercritical gas heater under various design and operating conditions. The study also examines the impact of heat exchanger design and operation on a transcritical biomass-CO_2 power generation system. The research findings can contribute to the optimal design of the heat exchanger and system control. Overall, this proposed and developed model can effectively determine the thermohydraulic characteristics of the heat exchangers and simulate their effects on the associated supercritical CO_2 heat-to-power conversion systems with high precision.

2. System description

Fig. 1 depicts the schematic diagram of an integrated system for biomass unit and CO_2 power generation, along with the thermodynamic cycles represented in T-S and P-H diagrams. The entire system comprises several critical components, such as a biomass CO_2 heater, a CO_2 shell-and-tube gas heater, a needle valve, two gas coolers, a recuperator, a compressor, and a water cooler. It is worth

noting that the needle valve and gas cooler-1 combination act as a CO_2 turbine simulator. The system is designed to operate using a CO_2 transcritical Brayton cycle, as depicted in Fig. 1. In this system, the high-temperature flue gas generated from the biomass combustion boiler flows through the CO_2 gas heater to directly heat the supercritical CO2 fluid to a high temperature. The CO_2 then undergoes an expansion process in the turbine simulator to generate power, and subsequently, releases heat to the recuperator. Following this, the CO_2 at subcritical pressure further releases heat through gas cooler-2, prior to entering the transcritical compressor for pressurization. The CO_2 then absorbs heat through the recuperator, before being reheated by the CO_2 gas heater. The cycle thus repeats. Some of the key parameters considered in the design of the system are the flue gas temperature of 800 °C, with a mass flow rate of 0.12 kg/s, the CO_2 turbine inlet temperature of 500°C, pressure of 120 bar, Due to the condition of high temperature heat source utilization, the supercritical CO_2 gas heater is considered. A mass flow rate of 0.1272 kg/s, and the CO_2 turbine outlet pressure of 50.871 bar are designed based on the saturated CO_2 temperature of 25 °C at compressor inlet, and also designed power generation of 11.9 kW.

The particular CO_2 gas heater is singled out and analysed purposely based on this designed operating condition.

3. Numerical analysis

3.1. Physical model

A geometrical model of the counterflow type supercritical CO_2 gas heater has been developed in three-dimensional (3D) form using SOLIDWORKS 2019, as illustrated in Fig. 2. Biomass flue gas flows through the shell side while CO_2 flows through the tubes. In order to simplify the modelling process, airflow has been used to represent the biomass flue gas. The CO_2 gas heater is composed of two baffles and 13 inner tubes, each with a tube length of 3.472m. The diameters of the shell pipe and tube are 101.6 mm and 13.7 mm, respectively. More geometrical details can be seen in Table 1. To comprehensively investigate and simulate the performance of this specific shell-and-tube heat

exchanger, various operating parameters such as CO_2 pressure, CO_2 mass flow rate, flue gas temperature and flue gas mass flow rate have been varied and applied.

3.2. Turbulence model

According to the turbulent flow involved in present study, it is imperative to account for the turbulence effects by utilizing an appropriate turbulence model. Therefore, the Realizable k-ε model has been employed for the model development and simulation, as it yields superior and accurate performance calculations for separation, rotation and recirculation flows. Moreover, k-ε model takes less computational time than the k-ω turbulence model [11]. Such advantages of the selected model have been substantiated by previous research findings reported in the relevant literature. Yang et al. [34] compared three different turbulence models for calculating fluid pressure drops and heat transfer coefficients in a shell-and-tube heat exchanger. The results revealed that the Realizable k-ε model exhibited higher accuracy when compared to experimental data. A similar conclusion was summarized by Ozden and Tari [12] in their study, where the Realizable k-ε model was implemented to predict fluid pressure drops and heat transfer coefficients in a STHX, and was found to provide more accurate results when compared to the Standard k-ε and Sparalt-Allmaras models. Therefore, in the present study, the Realizable k-ε model was used for all simulations.

3.3. Governing equations

The following assumptions are made for the CFD model development:

- Due to the complexity of flue gas compositions, it is difficult to get the thermophysical properties before detailed measurements are carried out. Therefore, airflow is selected to represent the biomass flue gas in the paper.
- There is no heat loss between the heat exchanger and ambient.
- Steady, compressible and turbulent fluid flows are assumed.

- CO_2 fluid properties are varied with both temperature and pressure.

The present section outlines governing equations employed in the CFD simulations, including continuity, momentum, energy conservation, turbulent kinetic energy and turbulent energy dissipation as detailed below [12,34].

Continuity equation:

$$\frac{\partial u_i}{\partial x_i} = 0 \tag{1}$$

Momentum equation:

$$\rho \frac{\partial u_i u_j}{\partial x_i} = -\frac{\partial P}{\partial x_i} + \mu \frac{\partial^2 u_i}{\partial u_j^2} \tag{2}$$

Energy equation:

$$\frac{\partial \rho u_i T}{\partial x_i} = \frac{\partial^2 T}{\partial x_i^2} \frac{K}{c_p} \tag{3}$$

Turbulent kinetic energy equation:

$$\frac{\partial}{\partial t}(\rho k) + \frac{\partial}{\partial x_j}(\rho k u_j) = \frac{\partial}{\partial x_j}\left[(\mu + \frac{\mu_t}{\sigma_k})\frac{\partial k}{\partial x_j}\right] + \Gamma - \varepsilon \tag{4}$$

Turbulent energy dissipation equation:

$$\frac{\partial}{\partial t}(\rho \varepsilon) + \frac{\partial}{\partial x_j}(\rho \varepsilon u_j) = \frac{\partial}{\partial x_j}\left[(\mu + \frac{\mu_t}{\sigma_\varepsilon})\frac{\partial \varepsilon}{\partial x_j}\right] + C_1 \Gamma \varepsilon - C_2 \frac{\varepsilon^2}{k + \sqrt{\nu \varepsilon}} \tag{5}$$

where $\Gamma = \mu_t \left(\frac{\partial u_i}{\partial x_j} + \frac{\partial u_j}{\partial x_i}\right)\frac{\partial u_i}{\partial x_i}$, $\mu_t = \rho C_\mu \frac{k^2}{\varepsilon}$.

The model constants $C_1, C_2, \sigma_k, \sigma_\varepsilon$ are defined as the following values:

$$C_1 = 1.44 \quad C_2 = 1.9 \quad \sigma_k = 1.0 \quad \sigma_\varepsilon = 1.2$$

3.4. Data reduction

The total heat transfer rates of shell and tube sides can be determined using Eq.(6) and Eq.(7) respectively.

$$Q_s = \dot{m}_s\left(H_{s,in} - H_{s,out}\right) \tag{6}$$

$$Q_t = \dot{m}_t\left(H_{t,out} - H_{t,in}\right) \tag{7}$$

Since no heat loss between the heat exchanger and ambient is assumed, the average heat transfer rate can thus be determined by Eq.(8):

$$Q_{av} = Q_s = Q_t \tag{8}$$

The overall heat transfer coefficient of the heat exchanger can be represented by the following equation, based on the outer surface area of tubes:

$$U = \frac{Q_{av}}{F \times L \times N_t \times \pi d_o \times \Delta T_m} \tag{9}$$

where, F is a correction factor to counterflow calculation for the heat exchanger, ΔT_m is the logarithmic mean temperature difference (LMTD) obtained by inlet and outlet fluid temperatures of both shell and tube sides.

$$\Delta T_m = \frac{(T_{s,in} - T_{t.out}) - (T_{s,out} - T_{t.in})}{ln(T_{s,in} - T_{t.out}) - ln(T_{s,out} - T_{t.in})} \tag{10}$$

The shell side fluid flow heat transfer coefficient can be obtained by utilizing Eq.(11).

$$h_s = \frac{1}{\frac{1}{U} - \frac{1}{h_t}\frac{d_o}{d_i} - \frac{d_o}{2k} ln\frac{d_o}{d_i}} \tag{11}$$

where h_t is the tube side heat transfer coefficient calculated from the CFD simulation.

The Fanning friction factor on tube-side f_t and Darcy-Weisbach friction factor on shell-side f_s can be obtained by Eq. (12) and Eq. (13) respectively.

$$f_t = \frac{\Delta P_t d_i}{2\rho u_{tm}^2 L} \tag{12}$$

$$f_s = \frac{2\Delta P_s D_e (\frac{\mu_b}{\mu_{wall}})^{0.14}}{(N_b + 1) D_s \rho u_{sm}^2} \tag{13}$$

where μ_b is the viscosity of the shell-side fluid at bulk temperature, and μ_{wall} is the viscosity of the tube-side fluid at wall temperature.

In order to calculate the tube and shell side fluid pressure drop ΔP_t and ΔP_s, the values of f_t and f_s can be determined using Eq. (14) [35-36] and Eq. (15) [22,25] respectively.

$$f_t = (1.58\, ln(Re_t) - 3.28)^{-2} \tag{14}$$

$$f_s = \exp(0.576 - 0.19\, ln(Re_s)) \qquad 400 < Re_s < 1 \times 10^6 \tag{15}$$

In present study, the tube side heat transfer coefficients derived by the CFD model are compared to those calculated by the Petukhov-Kirillow correlation represented by Eq.(16)[35-36].

$$Nu = \frac{(f_t/2)Re_t Pr}{12.7\sqrt{\frac{f_t}{2}}\left(Pr^{\frac{2}{3}}-1\right)+1.07} \qquad 0.5 < Pr < 2000, 10^4 < Re_t < 5 \times 10^6 \tag{16}$$

As previously mentioned, Kern and Bell-Delaware methods are widely accepted as the most accurate approaches for calculating the shell side heat transfer coefficient and pressure drop of a STHX. Therefore, in this study, these methods have been utilized to validate the developed CFD model.

$$\frac{h_{Kern,s}D_e}{k} = 0.36\left(\frac{D_e G_s}{\mu}\right)^{0.55}\left(\frac{c_p \mu}{k}\right)^{\frac{1}{3}}\left(\frac{\mu_b}{\mu_{wall}}\right)^{0.14} \tag{17}$$

$$h_{Bell-Delaware,s} = h_{id} J_c J_l J_b J_s J_r \tag{18}$$

where J_c, J_l, J_b, J_s, J_r are correction factors.

The ideal heat transfer coefficient, h_{id} for pure cross flow is given by:

$$h_{id} = j_i C_{ps}\left(\frac{m}{A_s}\right)(Pr)^{-\frac{2}{3}}\left(\frac{\mu_s}{\mu_{s,w}}\right)^{0.14} \tag{19}$$

The pressure drop can be calculated as:

$$\Delta P_{Bell-Delaware,s} = \Delta P_c + \Delta P_w + \Delta P_e \tag{20}$$

3.5. Grid independency test

The CO_2 gas heater was meshed in Ansys ICEM CFD 19.2 using hexahedral type elements, as illustrated in Fig. 2. In order to ensure the accuracy of the CFD simulation results, a grid independence test was conducted. This involved comparing the pressure drop and heat transfer coefficient calculations for the shell side using different numbers of grid cells. The results of this test are presented in Fig. 3. Five different mesh configurations, consisting of 2,286,926, 2,632,068, 3,057,565, 3,418,240, and 3,845,219 cells, were tested to achieve an optimized grid size for the CO_2 gas heater model. The results showed that the relative differences in shell-side fluid pressure drop and heat transfer coefficient calculations between the mesh sizes of 3,057,565 and 3,418,240 were both less than 1%. If the mesh number increases further to 3,845,219, the relative discrepancies for shell-side fluid pressure drop and heat transfer coefficient calculations with mesh numbers of 3,418,240 and 3,845,219 are 0.1% and 0.8% respectively. Taking into account the compromise between the model accuracy and computational time, the model with 3,057,565 cells is applied for the entire simulation cases.

3.6. Boundary conditions

In the present study, both the shell and tube sides are subjected to inlet boundary conditions of fluid temperatures and velocities, while fluid outlet boundary conditions are set as pressure outlets. The simulation operating conditions of the model are specified in Table 2. Specifically, the fluid pressure at the shell side outlet is set to atmospheric pressure, while the fluid pressures of the tube side outlet are varied between 8 and 28 MPa. The biomass flue gas temperatures range from 873.15 to 1273.15 K, with corresponding mass flow rates between 0.08 and 0.16 kg/s. Additionally, the CO_2 fluid mass flow rates vary from 0.08 to 0.16 kg/s, with temperatures ranging from 495 to 745 K. In order to examine the impact of various operational parameters on the performance of the shell-and-tube heat exchanger (STHX), a single variable is altered in each simulation, while all other parameters are held constant at their respective design values, as listed in Table 2. The thermophysical properties of CO_2 and airflow, such as density, viscosity, specific heat capacity, and thermal conductivity, are dependent on both temperature and pressure. These properties are calculated utilizing the REFPORP 8.0 software. These functions are programmed in C language using the Visual Studio 2017 platform. In ANSYS Fluent 19.2,

these properties are defined using the User Define Function (UDF). The Simple scheme is chosen for coupling the pressure and velocity fields. The convergence criterion is set with the energy residual of less than 10^{-7} and all other residuals of less than 10^{-3}.

4. Model results and validations

4.1. Validations

Prior to performing detailed computational fluid dynamics (CFD) simulations, a case was simulated based on the designed operating conditions, and the results were compared with those obtained from assigned empirical correlations. The Kern and Bell-Delaware methods are two most commonly used routines to calculate shell side fluid pressure drop and heat transfer coefficient of a shell-and-tube heat exchanger. Therefore, the CFD simulation results of shell side heat transfer and hydraulic parameters were compared with those calculated by Kern and Bell-Delaware methods, as depicted in Fig. 4(a). As illustrated in Fig. 4, the Reynolds number of flue gas on the shell-side ranges from 6211 to 14278 while the Reynolds number of CO_2 flow on the tube-side varies from 16791 to 34783. Both simulation and correlation results indicate that the heat transfer coefficient and pressure drop of flue gas both increase with higher Reynolds number. Moreover, as depicted in the figure, the maximum discrepancies between the simulation results and the Kern method calculations for flue gas heat transfer coefficient and pressure drop are 2.1% and 25% respectively, whereas the maximum discrepancies between simulation results and Bell-Delaware calculations for flue gas heat transfer coefficient and pressure drop are 4.6% and 7.6%, respectively. All the deviations are within acceptable ranges, it is noteworthy that the CFD model simulations are relatively consistent with those calculated by the Bell-Delaware method. This could further substantiate the appropriateness and precision of utilizing the Bell-Delaware method for the shell side fluid calculations of the STHX at the designated design conditions.

As indicated in Fig.4 (b), a comparison is made between the simulation results and the calculation results obtained from Petukhov-Kirillow empirical correlations [35], which are widely acknowledged for their reliability in predicting shell-and-tube heat exchanger tube side fluid heat transfer coefficient

and pressure drop. As demonstrated, a higher Reynolds number of CO_2 flow on the tube side results in higher heat transfer coefficient and pressure drop. The maximum deviations between the CFD simulation and empirical correlation results for tube side heat transfer coefficient and tube side pressure drop are found to be 4.9% and 4%, respectively. The simulation results are in good agreement with the empirical correlations. Moreover, the heating capacity of the heat exchanger is determined to be 34.24 kW by the validated CFD model at the designed operating condition, whereas the manufacturer's data reports a value of 26.86 kW. This comparison outcome can show the reasonable accuracy of the developed CFD model. Consequently, the validated model is capable of accurately predicting the heat transfer and hydraulic behaviours of the CO_2 gas heater.

4.2. Temperature contours

Fig.5 illustrates the temperature and velocity contours of the shell-and-tube heat exchanger at central plane under different flue gas mass flow rates, as obtained from the CFD simulation results. The impacts of shell side fluid mass flow rates on temperature distributions can be clearly observed. It shows that at each mass flow rate, the temperature of flue gas undergoes a gradual decrease from the inlet to the outlet, while the temperature of CO_2 experiences a progressive increase from the inlet to the outlet. The temperature of both flue gas and CO_2 outlets increase as the flue gas mass flow rate increases. This phenomenon is attributed to the higher velocity of flue gas, which improves the heat exchanger performance between hot and cold fluids, leading to an enhancement in the fluid heat transfer coefficient on the shell side. In quantity, Fig. 4 indicates that as the shell side fluid mass flow rate increases from 0.08 kg/s to 0.16 kg/s , the Reynolds number of the flue gas RE_{flue} changes from 6211 to 27444, and correspondingly, the shell side fluid heat transfer coefficient increases from 129.3 W/m^2K to 214.7 W/m^2K . The logarithmic mean temperature difference (LMTD) is a critical consideration in heat exchanger design, serving as a driving force for the transfer of heat from a hot fluid to a cold fluid. At flue gas mass flow rates of 0.08 kg/s, 0.12 kg/s, and 0.16 kg/s, the calculated LMTDs are 214.6 K, 225.9 K, and 230 K, respectively. However, an increase in the mass flow rate of the shell side fluid results in a corresponding increase in pressure drops. Subsequently, the flue gas pressure drops are 6569.97 Pa,

15205.20 Pa and 28353.50 Pa respectively respect to corresponding flue gas mass flow rates. Therefore, the rate of increase in pressure drop is significantly higher than that of the shell side heat transfer coefficient. It is well-established that a higher pressure drop requires more power consumption from the exhaust fan. Thus, an optimal flue gas mass flow rate should exist, which can improve the heat exchanger performance while avoiding the excessive energy consumption of the exhaust fan. In addition, the flue gas located between the CO_2 fluid inlet and flue gas outlet shows a relatively high temperature at flue gas mass flow rate of 0.12 kg/s, as depicted in Fig.5 (a)(b)(c). Lower mass flow rate of 0.08 kg/s with lower velocity can limit heat transfer rate between CO_2 and flue gas flows in this region, leading to the flue gas temperature determined mainly by CO_2 inlet temperature, as indicated in Fig.5 (d). It is shown in Fig. 5 (f), for the higher mass flow rate of 0.16 kg/s with high kinetic energy and high driving force, flue gas exits the outlet port directly, making the left stagnated region as near-vacuum state. In contrast, flue gas with adequate mass flow rate of 0.12 kg/s can partly reaches to the region between the CO_2 fluid inlet and flue gas outlet and thus has a higher temperature in that area compared to other two conditions.

Fig. 6 displays the temperature contours of two cross sections located immediately downstream of two baffles at flue gas flow rates of 0.08 kg/s, 0.12 kg/s and 0.16 kg/s. The figure demonstrates that, for each flue gas flow rate, the flue gas temperatures at the opening area of each baffle cross section are significantly greater than those observed at blocked area of the same cross section. This is due to the fact that stagnation area can be formed when flue gas flows after each baffle and less hot flue gas flows through that area. Besides, it is clearly shown that the average temperature of the cross-section is higher with higher flue gas mass flow rate due to less temperature decrease with a higher flue gas flow rate. Simulations have been carried out to determine the detailed flue gas and CO_2 temperature profiles averaged at each cross section along shell length direction (beginning with CO_2 flow inlet) are simulated and presented in Fig.7. The figure illustrates that the CO_2 fluid temperature experiences a smooth increase from its inlet to the outlet, except for a short distance between CO_2 flow inlet and flue gas outlet. This can be attributed to the stagnant flue gas present in that region. On the other hand, the flue gas temperature gradually decreases from its inlet to the outlet ports. However, a significant abrupt drop in temperature is observed at two specific sections located at 1.1 m and 2.2 m along the shell length

direction, just behind the two baffles. This behavior can be explained by the results shown in Figure 6. It reveals that as the velocity of flue gas increases, the temperature of flue gas at each cross sectional area exhibits a corresponding rise. Furthermore, the temperature of flue gas in the vicinity of the two stagnant ends is lower compared to that in the mainstream area. Additionally, an increase in the mass flow rate of flue gas leads to a corresponding rise in the temperature of CO_2 flow. This can be attributed to the fact that a higher mass flow rate of flue gas improves the heat transfer on the shell side of the heat exchanger, thereby increasing its heating capacity. Subsequently, the findings demonstrate that at flue gas mass flow rates of 0.08 kg/s, 0.12 kg/s and 0.16 kg/s, the outlet temperatures of CO_2 flow are 793.58 K, 838.9 K and 868.63 K, respectively, while the corresponding outlet temperatures of flue gas are 755.5 K, 812.7 K and 852.46 K.

4.3. Velocity distributions and streamlines

Fig. 8 illustrates the velocity distributions of flue gas at the inlet and outlet cross-sectional planes, corresponding to the three different flue gas mass flow rates. It is noteworthy that vortexes can be formed behind tubes at the inlet of flue gas flow. As illustrated, the regions between tubes across the second tube row from the top exhibit relatively higher velocities. It can be observed that an increase in mass flow rate results in higher velocity at top regions of the flue gas inlet. Flue gas traverses perpendicularly through the tube bundles with unevenly distributed velocities. At each demonstrated inlet plane (top row of the figure) , the lowermost portion of the cross-sectional area exhibits the minimum flue gas velocity. This in turn decreases the local heat transfer between shell and tubes, as the increased number of tubes in the direction of flue gas flow prevents adequate flue gas flow through the tube bundles. Moreover, the velocity at the bottom zones of the inlet cross-section plane is less affected by flue gas mass flow rate since flue gas continues to travel through the tubes towards the flue gas outlet. However, an increase in the flue gas mass flow rate has a greater impact on the velocity at the lowermost sections of the outlet cross-sectional area, owing to the location of the flue gas outlet, and consequently, it enhances the local heat transfer at these particular regions.

Fig.9 (a) displays the streamlines of flue gas flow through the tube bundles along shell. In the heat exchanger, baffles are utilized to suspend the tube bundles and direct the fluid flow on shell side along the tubes. The regions where the baffles are situated exhibit the highest flue gas velocity, Owing to the reductions of flue gas cross flow areas. Subsequently, recirculation zones are therefore formed when flue gas flow passes across each baffle, resulting in relatively lower flue gas velocities in these zones, since a portion of the flue gas flow stagnates and separates from the primary flue gas stream flowing through the tube bank. Despite the potential benefits of utilizing baffles in improving heat transfer behaviour, their implementation increases the pressure drop of shell-side fluid, resulting in an inevitable rise in the subsequent pumping power demand. Additionally, two stagnated regions for the shell-side flue gas flow exist: one located between the CO_2 fluid inlet and flue gas outlet, and the other situated between the flue gas inlet and CO_2 fluid outlet. The flue gas temperatures in these regions are relatively low, thereby resulting in insignificant heat transfer between the flue gas and CO_2 fluid. To enhance the heat transfer, it is recommended that the flue gas inlet and outlet ports be positioned as close as possible to each end of the heat exchanger. Therefore, to quantify the effects of stagnation regions and improve the thermal performance of the heat exchanger, a CFD model analysis was conducted on the shell-and-tube heat exchanger featuring different inlet and outlet port locations for the flue gas, as explained in the following model applications.

5. Model applications

5.1. Structural design optimization

Based on the simulation results of the CO_2 gas heater presented in section 4 and depicted in Fig. 9, it is evident that there exist two stagnated regions for the shell-side flue gas. The first stagnation zone is located between the CO_2 fluid inlet and flue gas outlet ports, whereas the second zone is between the flue gas inlet and CO_2 fluid outlet ports. The stagnant fluid in these regions tends to have a lower heat transfer coefficient due to reduced fluid motion, which can lead to lower heat transfer rates and reduced overall heat exchanger performance.

To enhance heat transfer in these regions, relocating the flue gas inlet and outlet ports may prove to be an effective approach, as illustrated in Fig.10. In order to differentiate between the two types of shell-and-tube heat exchangers, the original CO_2 gas heater is denoted as STHXA in this section, while the optimized gas heater is referred to as STHXB.

5.2. Temperature and streamline distributions

To investigate the impacts of different geometrical configurations, computational fluid dynamics (CFD) simulations are employed to model the STHXB. The resulting temperature distributions at the central lanes of the flue gas in STHXA and STHXB are compared, as depicted in Fig. 11. The analysis indicates that the relocation of the inlet and outlet ports of flue gas in STHXB effectively eliminates the temperature reduction observed at both ends of the shell side in STHXA. As a result of the optimization, the heat exchanger of STHXB is able to achieve a sufficient heat exchange area. This point also can be proved by Fig. 12, which illustrates that the temperature profile of flue gas in STHXB is slightly lower than that of STHXA in the central region, but significantly higher in the regions adjacent to two ends. Meanwhile, the CO_2 temperature profile on the tube side is found to be higher in the case of STHXB, implying a rise in heating capacity. Correspondingly, the LMTD of STHXB is computed as 203 K, whereas that of STHXA is 225.9 K. Although lower LMTD of STXHB can be calculated, much higher heat transfer coefficient of 214.4 W/(m^2K) for STHXB on shell side , compared to 171.4 W/(m^2K) of STHXA can be observed in Fig.14(a). Correspondingly, the heating capacity of STHXB is higher than that of STHXA, as shown in Fig.15(a). The reduced distances between CO_2 inlet and flue gas outlet, as well as between CO_2 outlet and flue gas inlet result in an enhanced heating capacity and thus a lower level of irreversibility in the heat transfer process.

Higher turbulence kinetic energy generally indicates a greater level of turbulence in a fluid flow. The relocations of flue gas inlet and outlet ports have resulted in regions at the two ends of the shell exhibiting higher kinetic energy, as demonstrated in Fig. 9 and Fig. 13. Consequently, it is evident that STHXB has higher turbulent kinetic energy than that of STHXA, which then has a greater turbulent

flow than that of STHXA. This is primarily attributed to the relocation of the inlet and outlet ports resulting in a higher mean velocity of flue gas.

Furthermore, it is observed in Fig.13 that the regions behind baffles are not utilized effectively for the heat transfer since the baffles tend to shift the direction of flue gas flow. However, the minimization recirculation zones can be achieved through an increase in the number of baffles or a decrease in the spacing between baffles.

5.3. Performance improvement for the heater

The thermal hydraulic performances of STHXA and STHXB were evaluated and compared using developed models. During each model simulation, a singular variable was altered while all other parameters remained constant at their respective designed values, as listed in Table 2. The findings displayed in Fig. 14(a) indicate an increase in both the shell-side heat transfer coefficient and pressure drop as a function of higher flue gas mass flow rates. In terms of heat transfer coefficients, STHXB exhibits average values that are 15.6% higher than those observed for STHXA across a range of flue gas mass flow rates, with a maximum increment of 25% observed at a flue gas mass flow rate of 0.12 kg/s. Regarding pressure drop, the STHXB is averagely 14% higher than that for STHXA. Both heat exchangers exhibit further pressure drop increase as the flue gas flow rate is increased.

The effectiveness of the shell-and-tube heat exchanger can be calculated as the ratio of actual heating capacity to the maximum heating capacity at a fixed operating condition as determined in Eq.(21):

$$\varepsilon = \frac{Q_{actual}}{Q_{max}} = \frac{Q_{actual}}{(mc_p)_{\min}(T_{flue,in} - T_{CO2,in})} \tag{21}$$

As depicted in Fig. 14(b), the effectiveness of both STHXA and STHXB diminishes with increasing flue gas mass flow rates; however, the rate of decrease becomes more gradual for flue gas mass flow rates above 0.12 kg/s. Nevertheless, the effectiveness of STHXB is always higher than that of STHXA, exhibiting an average increase of 7.8% when STHXB is employed. Fig. 14(c) depicts the changes in the effectiveness of the heat exchangers with an increase in the mass flow rate of CO_2. The results indicate that as the CO_2 mass flow rate increases from 0.08 kg/s to 0.12 kg/s, the effectiveness of both

STHXA and STHXB decreases. However, a further increase in the CO_2 mass flow rate to 0.16 kg/s leads to an increase in the effectiveness of both heat exchangers. This phenomenon is attributed to the rise in the thermal capacitance of the CO_2 side, which eventually reaches a value comparable to that of the shell side, resulting in an increase in the effectiveness of the heat exchanger system. On average, the effectiveness of STHXB is approximately 9.8% greater than that of STHXA, as shown in Fig.14(c).

Fig. 15 presents a comparison of the heating capacities of STHXA and STHXB at different operating conditions. The results indicate that the heating capacity of both heat exchangers increases with higher CO_2 mass flow rate, greater flue gas mass flow rate, and elevated flue gas temperature. Under constant operating parameter, the heating capacity of STHXB is always higher than that of STHXA. Fig. 15(a) illustrates that by changing the flue gas temperature and CO_2 mass flow rate, the heating capacity of STHXB can be enhanced by 9.2% in comparison to STHXA. Similarly, Fig. 15(b) demonstrates that, on average, the heating capacity of STHXB increases by 7.2% compared to STHXA when varying the flue gas temperature and flow rate. Fig. 15(c) reveals that by altering the flue gas temperature and CO_2 pressure, the heating capacity of STHXB can be enhanced by an average of 5.9% as compared to STHXA. While the CO_2 pressure has a negligible impact on the heating capacity of both heat exchangers, the performance analysis presented in this study demonstrates that the STHXB outperforms the STHXA in terms of heat transfer coefficient, effectiveness, and heating capacity at a fixed operating condition.

5.4. Performance improvement for the system

This study includes an investigation of the impact of CO_2 gas heater designs and operations on the performance of the corresponding system. To facilitate such an investigation, the CFD modeling simulation results were used to develop correlations between the CO_2 outlet temperature and the CO_2 inlet temperature, flue gas mass flow rate, and CO_2 pressure at turbine inlet. These correlations are presented as Eqs. (22) and (23), which can be used in the entire system simulations at different flue gas mass flow rate and various CO_2 pressure at turbine inlet respectively. It is found from the simulation results that when the CO_2 pressure at turbine inlet is fixed, the CO_2 outlet temperature is mainly affected

by the CO_2 inlet temperature and flue gas mass flow rate , as listed in EQ. (22). Similarly, at a fixed flue gas mass flow rate, the CO_2 outlet temperature relates closely with the CO_2 inlet temperature and CO_2 pressure at turbine inlet , as listed in EQ. (23). The corresponding correlative coefficients of c_1~c_6 at varied flue gas mass flow rate and CO_2 turbine inlet pressure are listed in Tables 3 and 4 respectively.

$$T_{CO2,out} = c_1 * T_{co2,in}^2 + c_2 * T_{co2,in} + c_3 * T_{co2,in} * \dot{m}_{flue} + c_4 * \dot{m}_{flue} + c_5 * \dot{m}_{flue}^2 + c_6 \quad (22)$$

$$T_{CO2,out} = c_1 * T_{co2,in}^2 + c_2 * T_{co2,in} + c_3 * T_{co2,in} * P_{CO2} + c_4 * P_{CO2} + c_5 * P_{CO2}^2 + c_6 \quad (23)$$

The thermal efficiency of a biomass-CO_2 power generation system can be indirectly affected by the performance of the shell-and-tube heat exchanger under different operating conditions and structural designs. In order to gain a complete understanding of this influence, a thermodynamic model for the biomass-CO_2 system has been developed using Engineering Equation Solver (EES) software. This model integrates the established CFD model and investigates the impact of turbine inlet pressure and heat source mass flow rate on the overall system performance. The integrated model is based on the following assumptions:

- The system operates under steady state;
- The kinetic and potential energies are neglected for the CO_2 flowing through the system components;
- These is no pressure drop for the CO_2 flowing through the recuperator or the second gas cooler;
- Flue gas inlet temperature is 1073.15 K;
- Mass flow rate of CO_2 is 0.1272 kg/s;
- Cooling water is applied as heat sink and its temperature is 288.15 K;
- Temperature difference between compressor inlet and cooling water is 10 K;
- Turbine outlet pressure is 5.0871 MPa;
- Isentropic efficiency of turbine and effectiveness of recuperator are both assumed as 0.8;
- Compressor isentropic efficiency is calculated based on performance data from manufacturer;
- The dead states of pressure and temperature are assumed as atmospheric pressure and ambient air temperature respectively.

The system thermal efficiency can be calculated as follow:

$$\eta_{th} = \frac{W_{net}}{Q_{in}} = \frac{W_{turbine} - W_{compressor}}{Q_{in}} \quad (24)$$

The thermal efficiency of the initial STHXA can be observed in Fig. 16, demonstrating a positive correlation between temperature and thermal efficiency. Upon elevating the flue gas temperature from 873.15 K to 1073.15 K, a significant enhancement in thermal efficiency is observed. However, it is noteworthy that a further increase in temperature may lead to a decrease in the rate of improvement in thermal efficiency. Moreover, based on the results presented in Fig. 17, it can be observed that an increase in flue gas flow rate leads to an increase in the thermal efficiency of the integrated system, which includes either STHXA or STHXB. This can be attributed to the increased heat capacity of the gas heater. However, the extent of this increase in thermal efficiency decreases as the flue gas flow rate is further increased. While CO_2 pressure has a negligible effect on gas heater heat capacity, there exists an optimal CO_2 pressure that maximizes the thermal efficiency of system. This is due to the opposite effects of the CO_2 pressure at the turbine inlet on the turbine power generation and compressor power consumption when the CO_2 pressure at the turbine outlet is fixed. These simulation results can provide valuable insights for gas heater and system controls. Furthermore, integrating STHXB can lead to improved performance of the associated system. Specifically, when the flue gas mass flow rate is the only variable, the average thermal efficiency can be approximately 6% higher for the system with STHXB.

6. Conclusions

A detailed 3D CFD model was developed and validated for a shell-and-tube supercritical CO_2 gas heater used in a biomass-CO_2 power generation system. Realizable k-ε model was utilized for the simulations. The validated model was subsequently utilized to predict the thermal-hydraulic performance of the heat exchanger and its associated system at varying operating conditions and structural designs. Results indicate that the positioning of flue gas inlet and outlet ports can significantly

impact the heat transfer of the heat exchanger. The performance simulation and analyses reveal the following key findings:

- The augmentation of mass flow rate on both the shell and tube sides leads to an increase in heat transfer coefficient and pressure. The validation of the shell side thermal-hydraulic performance was conducted through the application of Kern and Bell-Delaware methods. The results demonstrated that the Bell-Delaware method is capable of predicting pressure drop with greater accuracy compared to the Kern method.
- If locations of flue gas inlet and outlet ports are far away from the ends of shell, stagnated zones can be formed. These zones are characterized by lower velocities, resulting in lower heat transfer coefficients and reduced heat transfer rates in these regions.
- It is observed that the velocity of fluid flow is increased after passing through a baffle. However, it is also noted that recirculation zones are formed behind each baffle, resulting in lower fluid velocities and ineffective utilization of these regions.
- It is found that heating capacity of the heat exchanger can be enhanced by elevating the flue gas temperature, flue gas mass flow rate, and CO_2 mass flow rate. However, the impact of CO_2 pressure on the heat exchanger heating capacity was found to be insignificant.
- Both flue gas mass flow rate and CO_2 pressure affect significantly on the system thermal efficiency which can be considered in the system optimal control strategies. The rate of increase in thermal efficiency slows down with increasing flue gas mass flow rate. Furthermore, there exits an optimal CO_2 pressure to maximize the system thermal efficiency.
- Through relocating the flue gas inlet and outlet ports of shell-and-tube heat exchanger (STHXB), the shell side heat transfer coefficient, effectiveness and heating capacity of heat exchanger can be effectively improved. Quantitively, when STHXB is applied to replace for STHXA, the heat exchanger effectiveness, heating capacity and system thermal efficiency can be improved about 7.8%, 5.9% and 6% respectively. In spite of the higher power consumption of the exhaust fan, the increase in pressure drop is still less than that of the heat transfer coefficient. Consequently, it can be concluded that the STHXB exhibits superior performance

compared to the original CO_2 gas heater STHXA, resulting in an enhanced thermal efficiency of the associated system.

- The application of detailed CFD modelling is a promising approach for gaining comprehensive insights into the performance of shell-and-tube heat exchangers. The simulation outcomes provide valuable inputs for the design and optimization of the heat exchanger, as well as for the control and operation strategies of the corresponding biomass-CO_2 power generation system.

Acknowledgements

The authors would like to acknowledge the support received from Ashwell Biomass Ltd, Research Councils UK (RCUK, EP/R000298/1) and Innovate UK for this research project.

References

[1] Saidur R, Abdelaziz EA, Demirbas A, Hossain MS, Mekhilef S. A review on biomass as a fuel for boilers. Renewable and sustainable energy reviews 2011; 15 :2262-2289.

[2] Ge YT, Li L, Luo X, Tassou SA. Performance Evaluation of a Low-grade Power Generation System with CO_2 Transcritical Power Cycles. Applied Energy 2018; 227:220-230.

[3] Li L, Ge YT, Luo X, Tassou SA. Experimental analysis and comparison between CO2 transcritical power cycles and R245fa organic Rankine cycles for low-grade heat power generations. Applied Thermal Engineering 2018; 136 :708–717.

[4] Padilla R, Too Y, Benito R, McNaughton R, Stein W. Thermodynamic feasibility of alternative supercritical CO2 Brayton cycles integrated with an ejector. Applied Energy 2016; 169: 49-62.

[5] Brun K, Friedman P, Dennis R. Fundamentals and applications of supercritical carbon dioxide (sCO2) based power cycles. Woodhead publishing 2017.

[6] Pekdemir T, Davies TW, Haseler LE, Diaper AD. Pressure drop measurements on the shell side of a cylindrical shell-and-tube heat exchanger. Heat transfer engineering 1994; 15:42-56.

[7] Gay B, Mackley NV, Jenkins JD. Shell-side heat transfer in baffled cylindrical shell-and tube exchangers—an electrochemical mass-transfer modelling technique. International Journal of Heat and Mass transfer 1976; 19 : 995-1002.

[8] Kim WK, Aicher T. Experimental investigation of heat transfer in shell-and-tube heat exchangers without baffles. Korean Journal of Chemical Engineering 1997; 14:93-100.

[9] Li H, Kottke V. Local heat transfer in the first baffle compartment of the shell-and-tube heat exchangers for staggered tube arrangement. Experimental thermal and fluid science 1998; 16 : 342-348.

[10] He Z, Fang X, Zhang Z, Gao X. Numerical investigation on performance comparison of non-Newtonian fluid flow in vertical heat exchangers combined helical baffle with elliptic and circular tubes. Applied Thermal Engineering 2016; 100:84-97.

[11] Pal E, Kumar I, Joshi JB, Maheshwari NK. CFD simulations of shell-side flow in a shell-and-tube type heat exchanger with and without baffles. Chemical Engineering Science 2016; 143 : 314-340.

[12] Ozden E, Tari I. Shell side CFD analysis of a small shell-and-tube heat exchanger. Energy Conversion and Management 2010; 51; 1004-1014.

[13] Halle H, Chenoweth JM, Wambsganss MW. Shell side waterflow pressure drop distribution measurements in an industrial-sized test heat exchanger. J. Heat Transfer 1988; 110:60-67.

[14] Sparrow EM, Reifschneider LG. Effect of interbaffle spacing on heat transfer and pressure drop in a shell-and-tube heat exchanger. International journal of heat and mass transfer 1986; 29 : 1617-1628.

[15] Abeykoon C. Compact heat exchangers–Design and optimization with CFD. International Journal of Heat and Mass Transfer 2020;146:118766.

[16] El Maakoul A, Laknizi A, Saadeddine S, El Metoui M, Zaite A, Meziane M, Abdellah AB. Numerical comparison of shell-side performance for shell and tube heat exchangers with trefoil-hole, helical and segmental baffles. Applied Thermal Engineering 2016; 109:175-185.

[17] Kunwer R, Pandey S, Bhurat SS. Comparison of selected shell and tube heat exchangers with segmental and helical baffles. Thermal Science and Engineering Progress 2020; 20 :100712.

[18] Kral D, Stehlik P, Van Der Ploeg HJ, Master BI. Helical baffles in shell-and-tube heat exchangers, Part I: Experimental verification. Heat transfer engineering 1996; 17: 93-101.

[19] Xu X, Zhang Y, Liu C, Zhang S, Dang C. Experimental investigation of heat transfer of supercritical CO_2 cooled in helically coiled tubes based on exergy analysis. International Journal of Refrigeration. 2018 May 1;89:177-85.

[20] Bell KJ. Delaware method for shell side design. Heat exchangers: thermal-hydraulic fundamentals and design. Hemisphere 1981; 581- 618.

[21] Kern DQ. Process heat transfer (Vol. 5). New York: McGraw-Hill 1950.

[22] Gaddis ES, Gnielinski V. Pressure drop on the shell side of shell-and-tube heat exchangers with segmental baffles. Chemical Engineering and Processing: Process Intensification 1997; 36 :149-159.

[23] Jayachandriah B, Vinay V. Design of helical baffle in shell and tube heat exchanger and comparing with segmental baffle using kern method. International Journal of Emerging Technology in Computer Science & Electronics 2015; 13 : 157-162.

[24] Shinde S, Chavan U. Numerical and experimental analysis on shell side thermo-hydraulic performance of shell and tube heat exchanger with continuous helical FRP baffles. Thermal Science and Engineering Progress 2018; 5 :158-171.

[25] Bayram H, Sevilgen G. Numerical investigation of the effect of variable baffle spacing on the thermal performance of a Shell and tube heat Exchanger. Energies 2017; 10 :1156.

[26] Chai L, Tassou SA. Performance Analysis of Heat Exchangers and Integrated Supercritical CO2 Brayton Cycle for Varying Heat Carrier, Cooling and Working Fluid Flow Rates. Heat Transfer Engineering. 2022 Oct 28:1-21.

[27] Chai L, Tassou SA. Modeling and evaluation of the thermohydraulic performance of compact recuperative heat exchangers in supercritical carbon dioxide waste heat to power conversion systems. Heat Transfer Engineering. 2022 Jul 20;43(13):1067-82.

[28] Zhang H, Guo J, Huai X, Cheng K, Cui X. Studies on the thermal-hydraulic performance of zigzag channel with supercritical pressure CO2. The Journal of Supercritical Fluids. 2019 Jun 1;148:104-15.

[29] Jiang Y, Liese E, Zitney SE, Bhattacharyya D. Optimal design of microtube recuperators for an indirect supercritical carbon dioxide recompression closed Brayton cycle. Applied Energy 2018 216:634-48.

[30] Ehsan MM, Guan Z, Klimenko AY, Wang X. Design and comparison of direct and indirect cooling system for 25 MW solar power plant operated with supercritical CO_2 cycle. Energy Conversion and Management 2018;168:611-28.

[31] Fourspring PM, Nehrbauer JP. The Variation in Effectiveness of Low-Finned Tubes Within a Shell-and-Tube Heat Exchanger for Supercritical CO_2. InInternational Conference on Nuclear Engineering 2012 Jul 30 (Vol. 44960, pp. 753-757). American Society of Mechanical Engineers.

[32] Cai HF, Jiang YY, Wang T, Liang SQ, Guo C, Zhu YM. An optimization of microtube heat exchangers for supercritical CO_2 cooling based on numerical and theoretical analysis. International Communications in Heat and Mass Transfer 2021;127:105532.

[33] Marchionni M, Bianchi G, Tassou SA. Review of supercritical carbon dioxide (sCO_2) technologies for high-grade waste heat to power conversion. SN Applied Sciences 2020; 2(4):1-3.

[34] Yang D, Khan T, Al-Hajri E, Ayub Z, Ayub A. Geometric optimization of shell and tube heat exchanger with interstitial twisted tapes outside the tubes applying CFD techniques. Applied Thermal Engineering 2019; 152:559-572.

[35] Petukhov BS, Genin LG, Kovalev S. Heat transfer in nuclear power plants. Moscow: Atomizdat, 367 p., 1974.

[36] Sleicher CA, Rouse MW. A convenient correlation for heat transfer to constant and variable property fluids in turbulent pipe flow. International Journal of Heat and Mass Transfer. 1975 May 1;18(5):677-83.

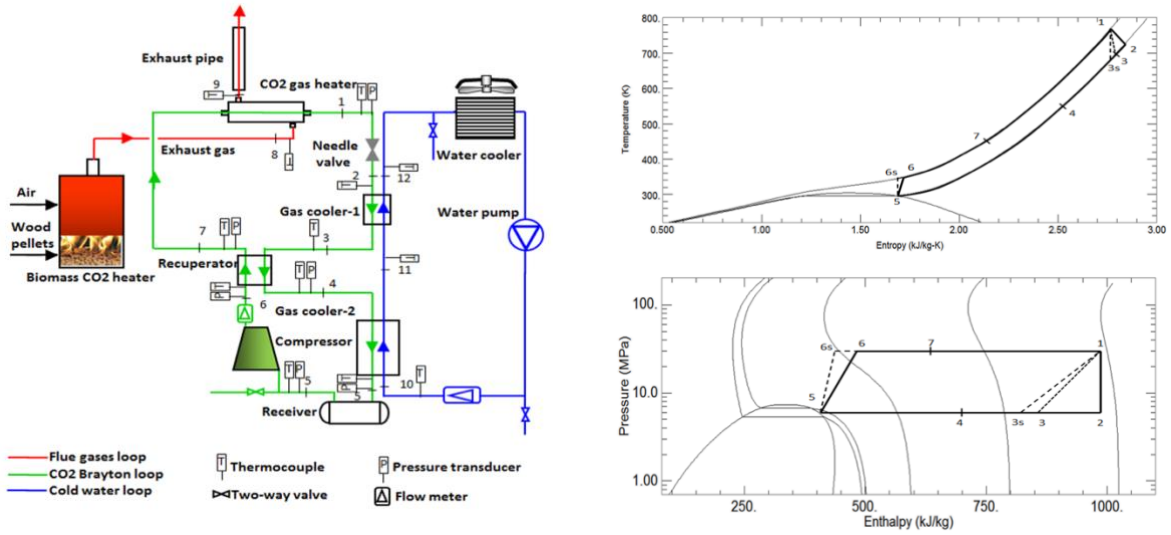

Fig. 1. Schematic diagram of integrated biomass unit and CO_2 power generation system and corresponding cycles shown in T-S and P-H diagrams.

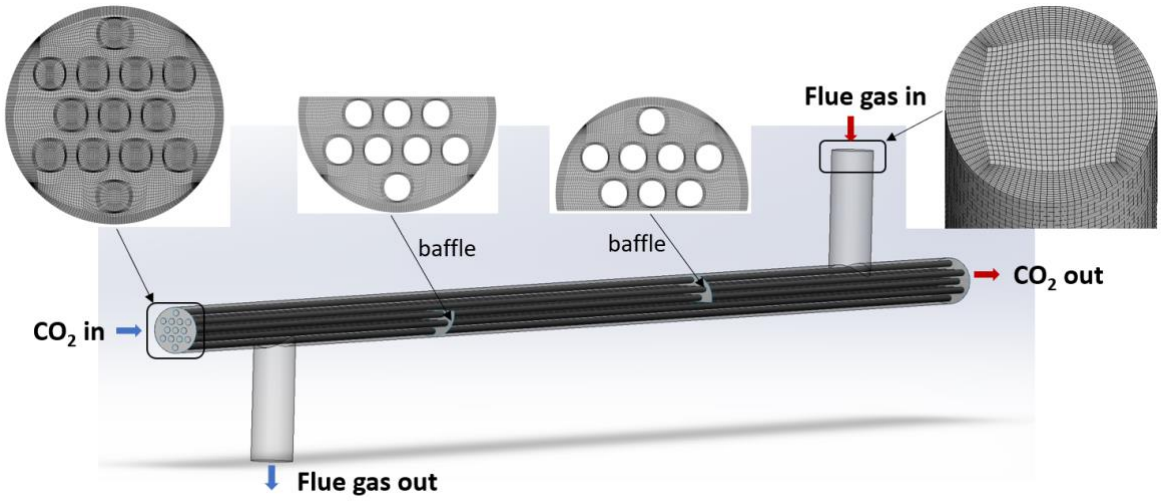

Fig. 2. The physical and mesh model of the simulated shell-and-tube heat exchanger.

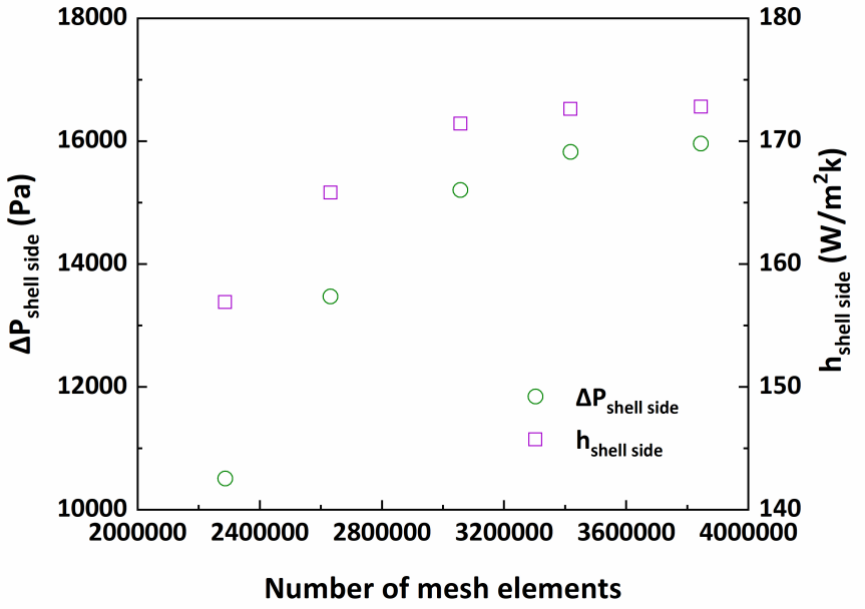

Fig. 3. Variations of pressure drop and heat transfer coefficient of shell side with different mesh sizes.

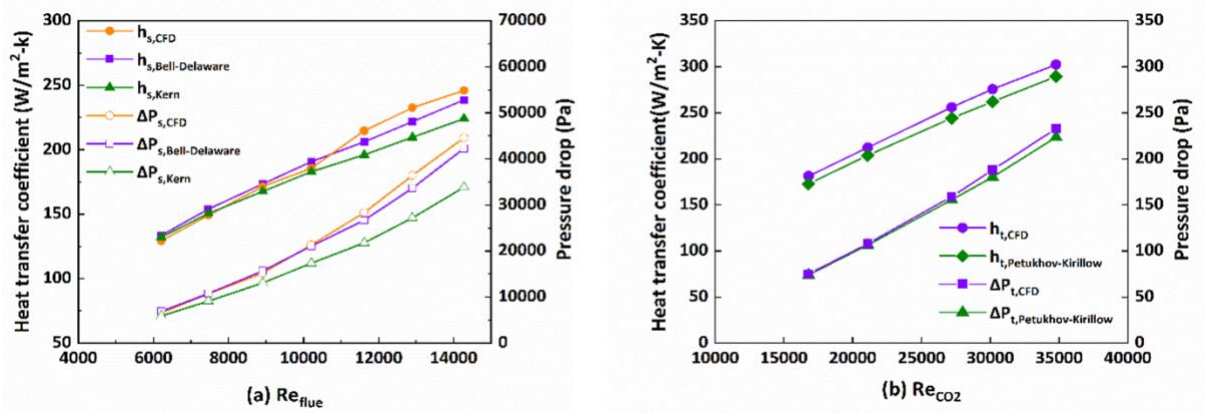

Fig. 4. Comparisons of shell and tube side heat transfer coefficients and pressure drops with empirical correlations.

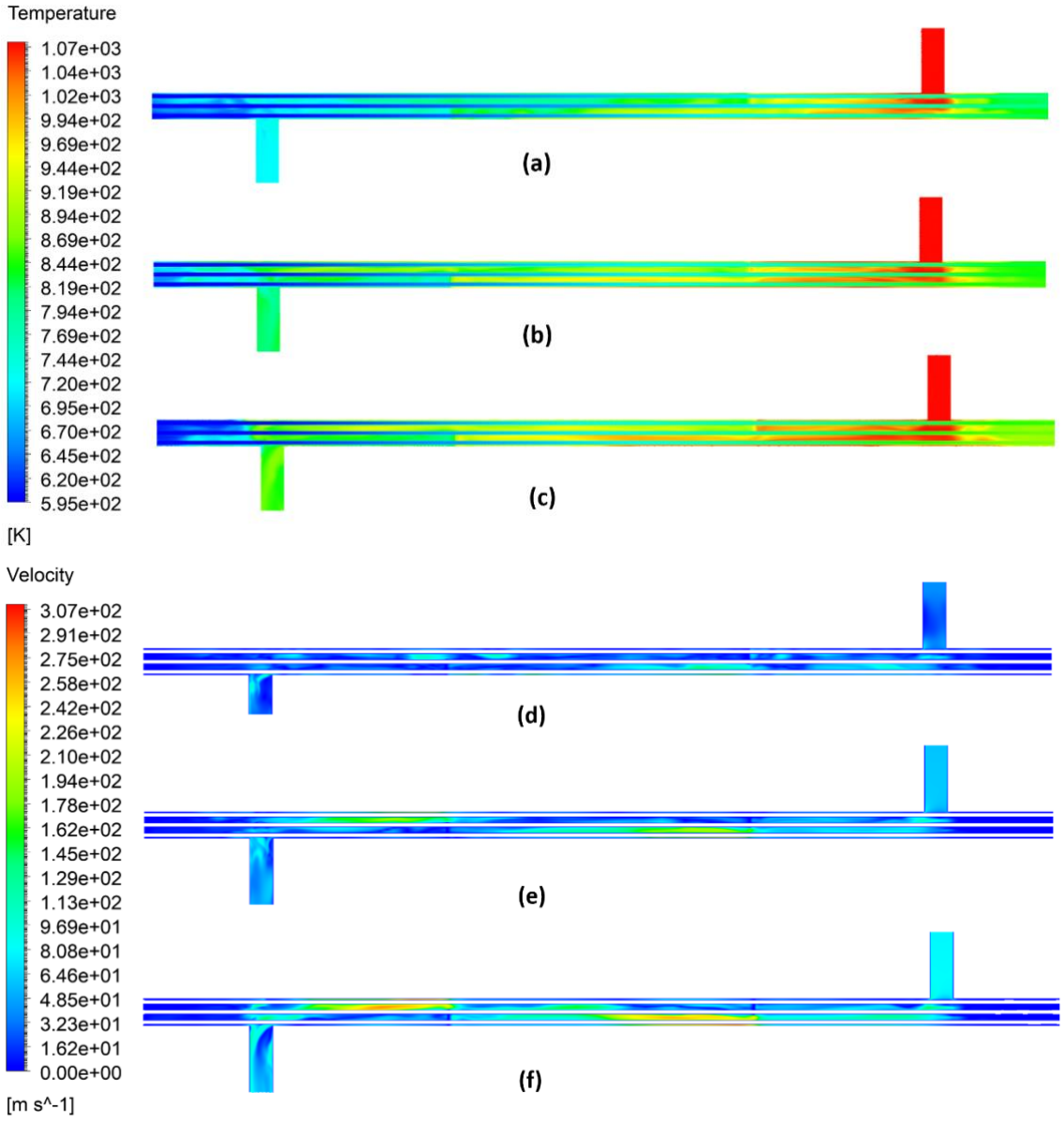

Fig. 5. Temperature contours gas heater and velocity contours of flue gas at central x-axial plane for flue gas mass flow rate: (a) (d) 0.08 kg/s; (b) (e) 0.12 kg/s; (c) (f) 0.16 kg/s. ($T_{flue\ gas} = 1073.15\ K, m_{CO2} = 0.1272\ kg/s, P_{CO2} = 12\ MPa$)

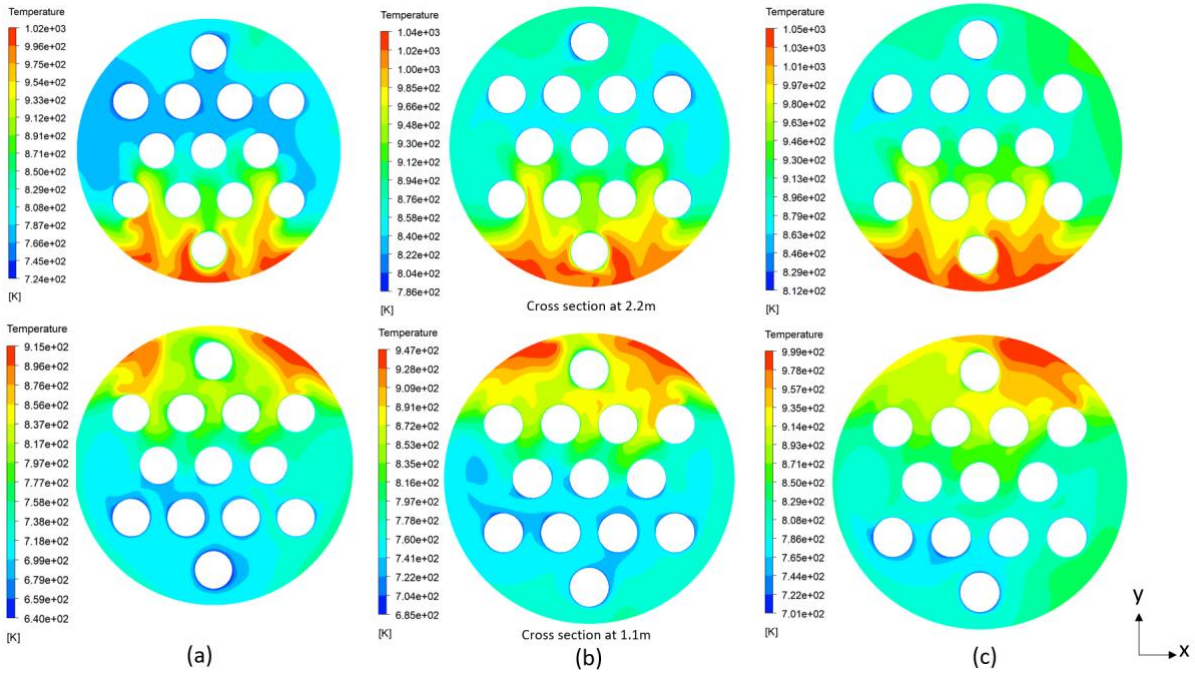

Fig. 6. Temperature contours of flue gas at cross sections of 1.1m and 2.2m along the shell tube direction for flue gas mass flow rate: (a) 0.08 kg/s; (b) 0.12 kg/s; (c) 0.16 kg/s. ($T_{flue\ gas} = 1073.15\ K, m_{CO2} = 0.1272\ kg/s, P_{CO2} = 12\ MPa$).

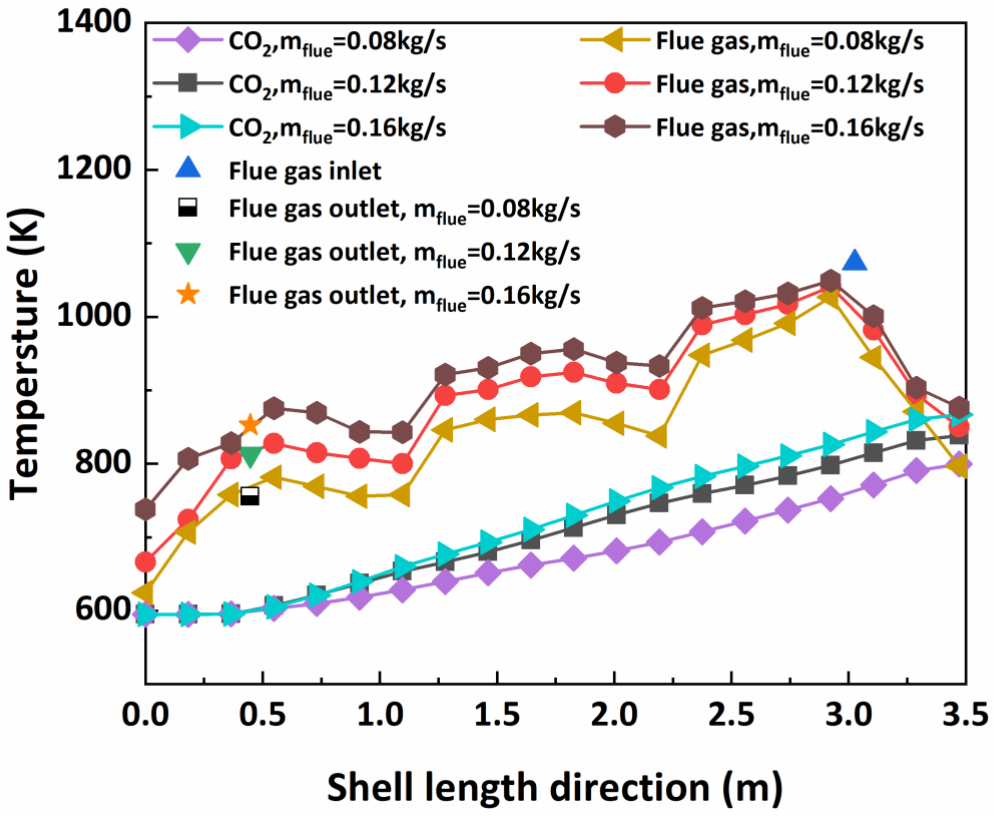

Fig. 7. CO_2 and flue gas temperature profiles along shell length direction at different flue gas mass flow rate.

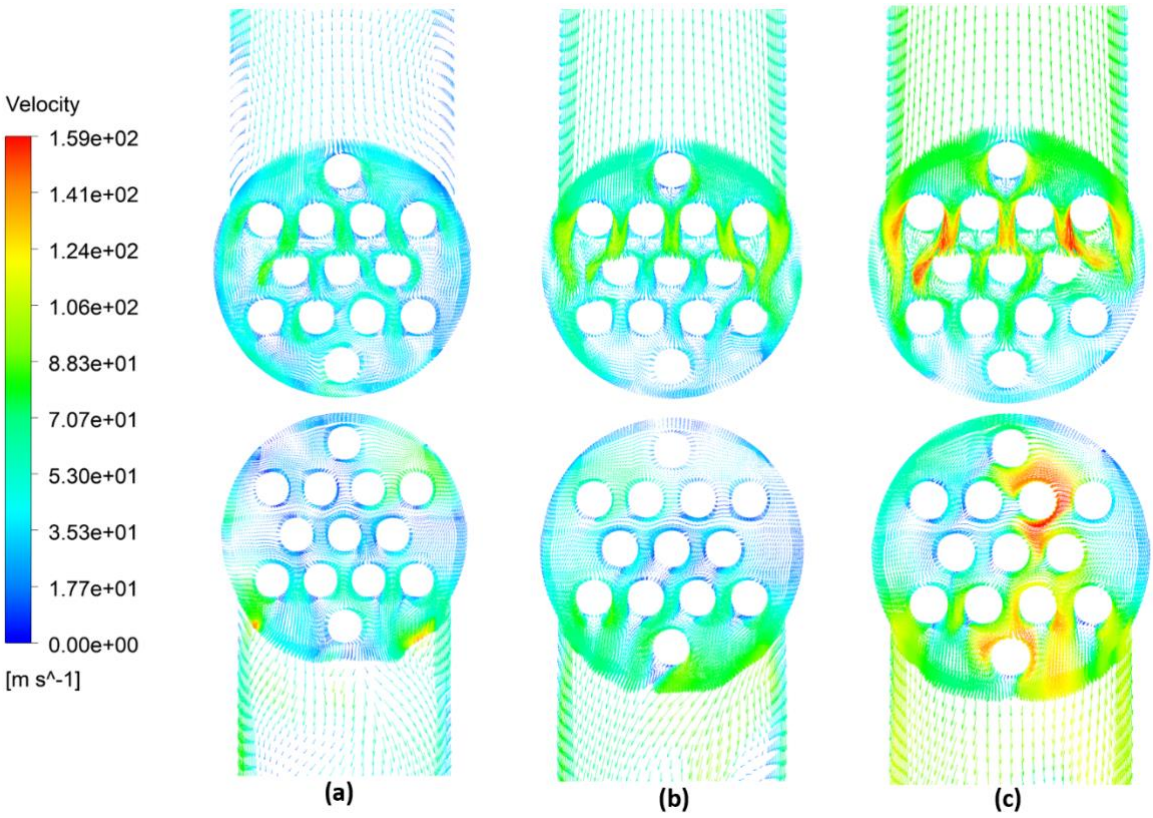

Fig. 8. Velocity distributions at inlet and outlet planes at flue gas mass flow rate of: (a)0.08 kg/s; (b) 0.12 kg/s; (c) 0.16 kg/s. ($T_{flue\ gas} = 1073.15\ K, m_{CO2} = 0.1272\ kg/s, P_{CO2} = 12\ MPa$)

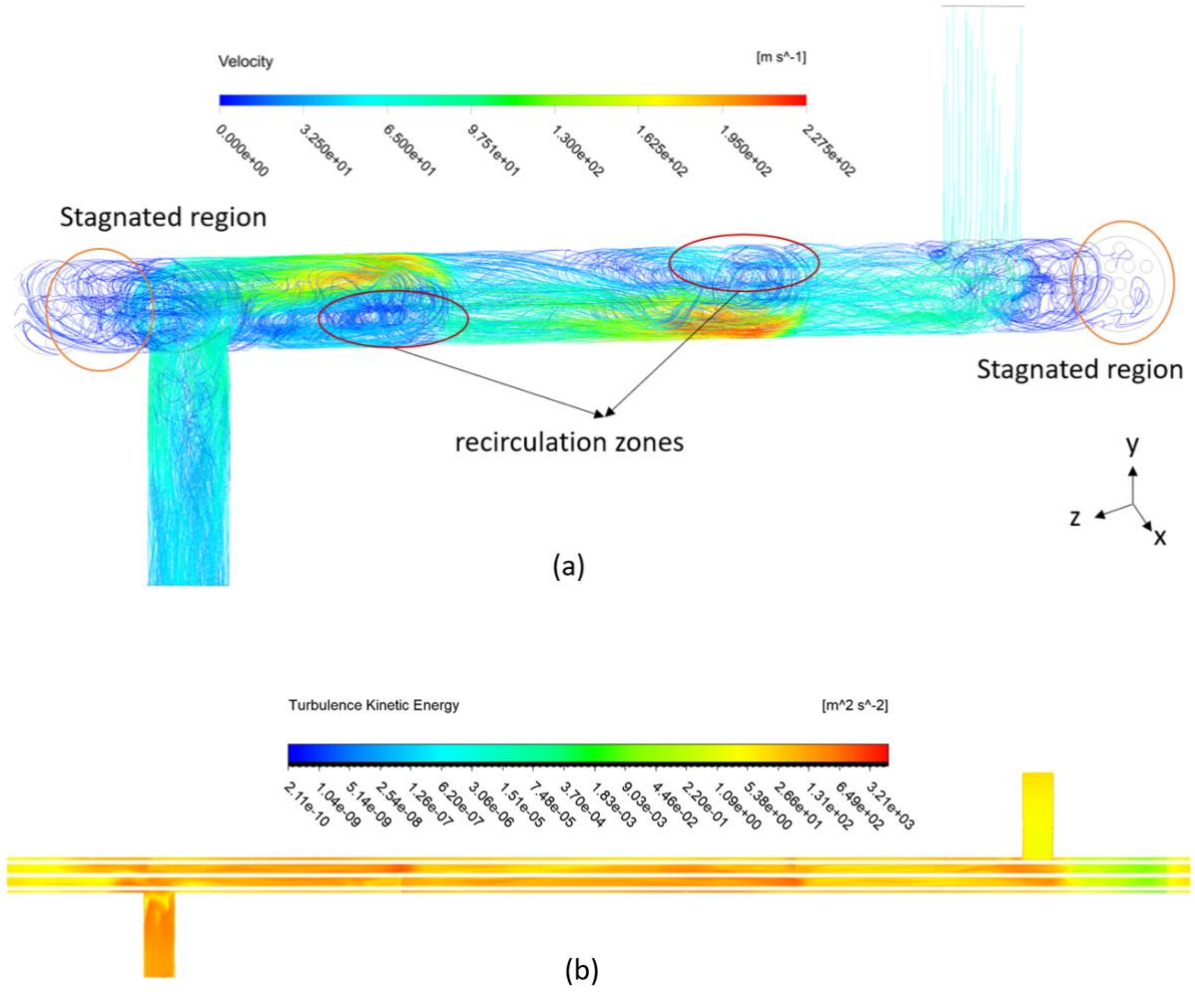

Fig. 9. (a) Velocity streamlines shell side flue gas and (b) turbulence kinetic energy of the central plane. ($m_{flue} = 0.12\ kg/s, _{flue\ gas} = 1073.15\ K, m_{CO2} = 0.1272\ kg/s$, $P_{CO2} = 12\ MPa$)

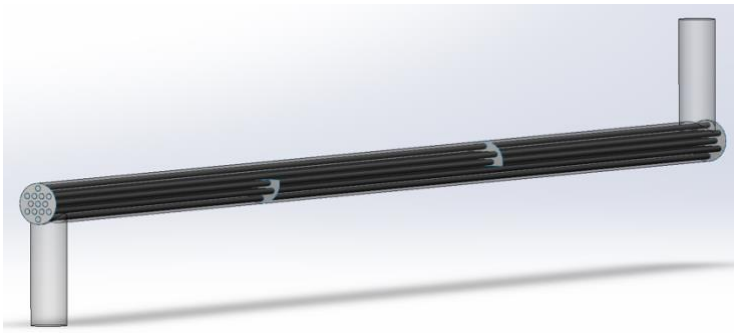

Fig. 10. Geometry for the relocated pipe ports of CO_2 gas heater (STHXB).

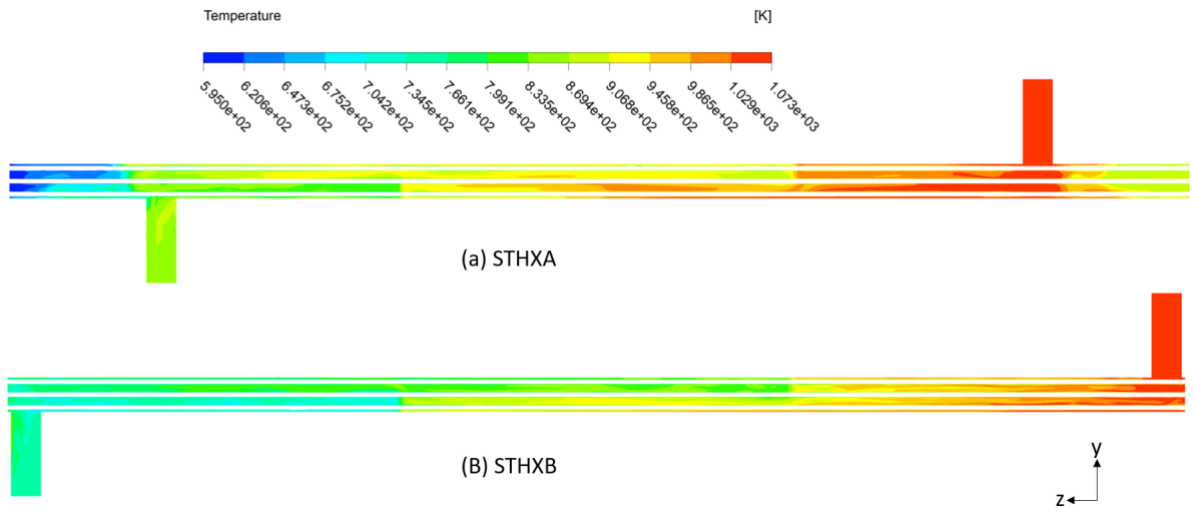

Fig. 11. Temperature contours at central x-axial plane of: (a) STHXA; (B) STHXB. (Operating conditions: $T_{flue\ gas} = 1073.15\ K, m_{flue\ gas} = 0.12\ kg/s,\ m_{CO2} = 0.1272\ kg/s, P_{CO2} = 12\ MPa$)

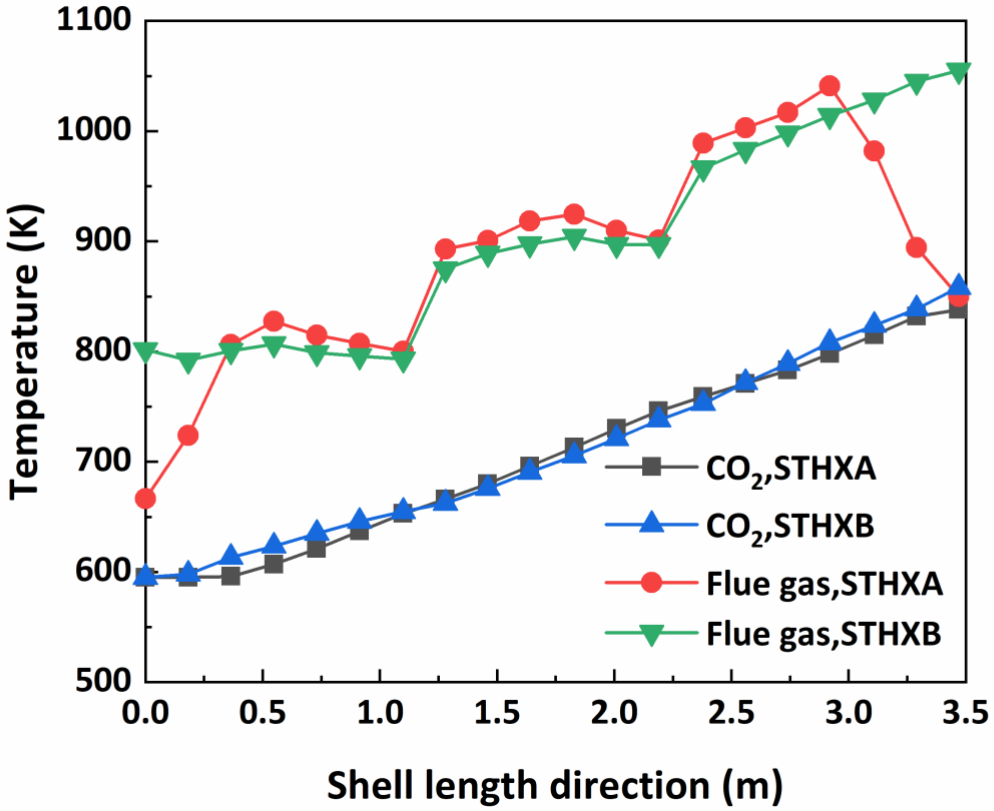

Fig. 12. Comparison of CO_2 and flue gas temperature profiles for STHXA and STHXB. (Operating conditions: $T_{flue\ gas} = 1073.15\ K, m_{flue\ gas} = 0.12\ kg/s,\ m_{CO2} = 0.1272\ kg/s, P_{CO2} = 12\ MPa$)

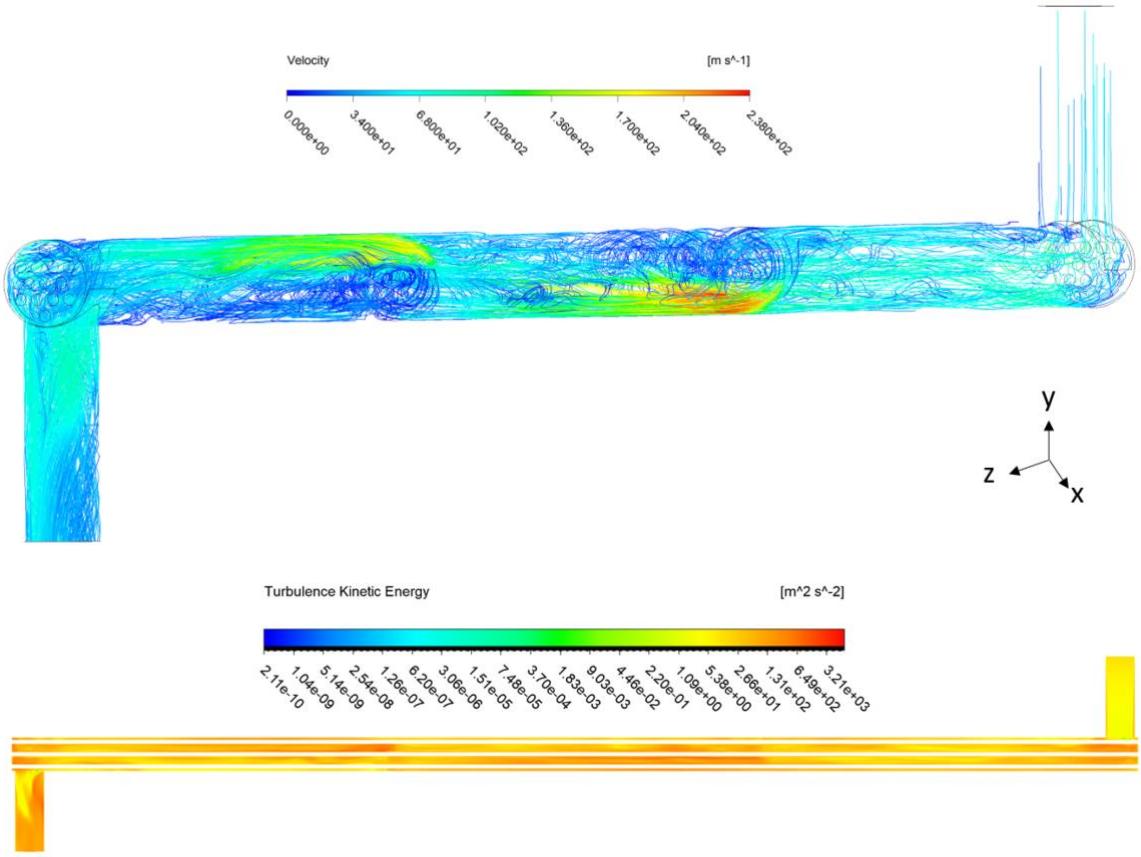

Fig. 13. velocity streamlines of shell side flue gas of STHXB and turbulence kinetic energy of the central plane. (Operating conditions: $T_{flue\ gas} = 1073.15\ K, m_{flue\ gas} = 0.12\ kg/s,\ m_{CO2} = 0.1272\ kg/s, P_{CO2} = 12\ MPa$)

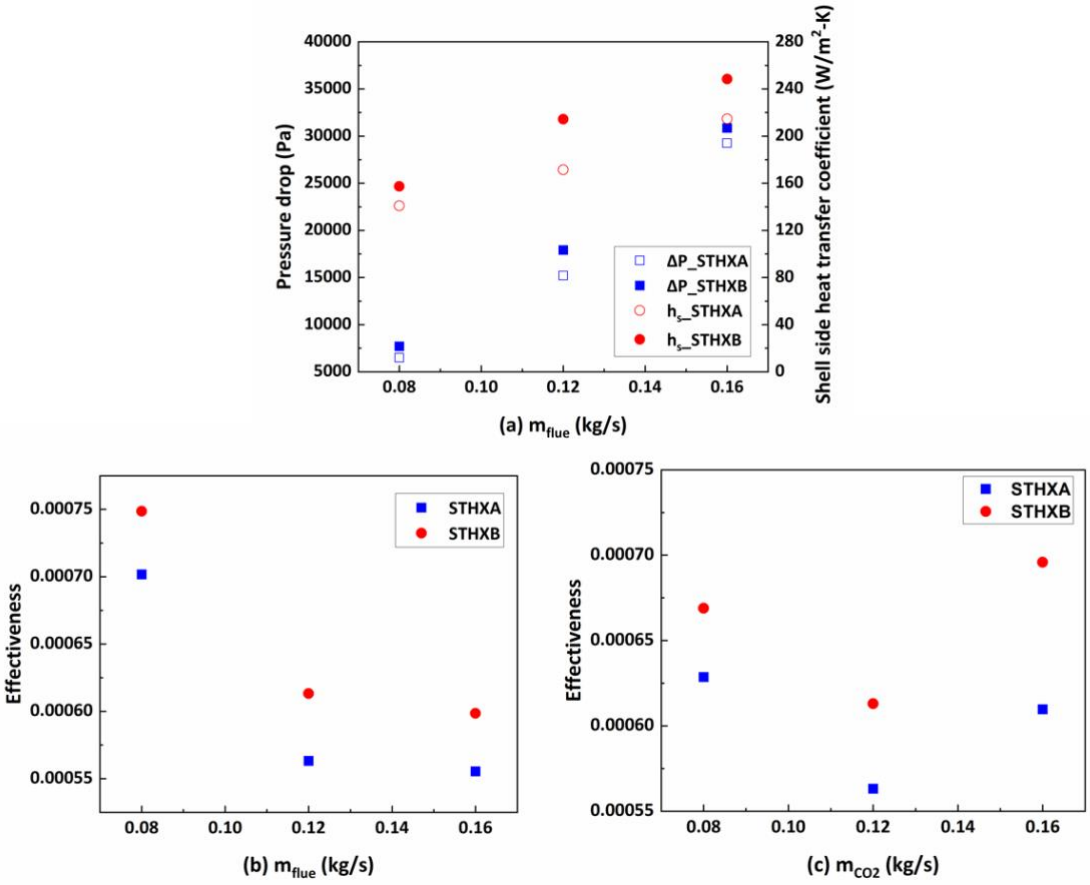

Fig. 14. Comparisons of heat transfer coefficient, pressure drop and effectiveness of STHXA and STHXB.

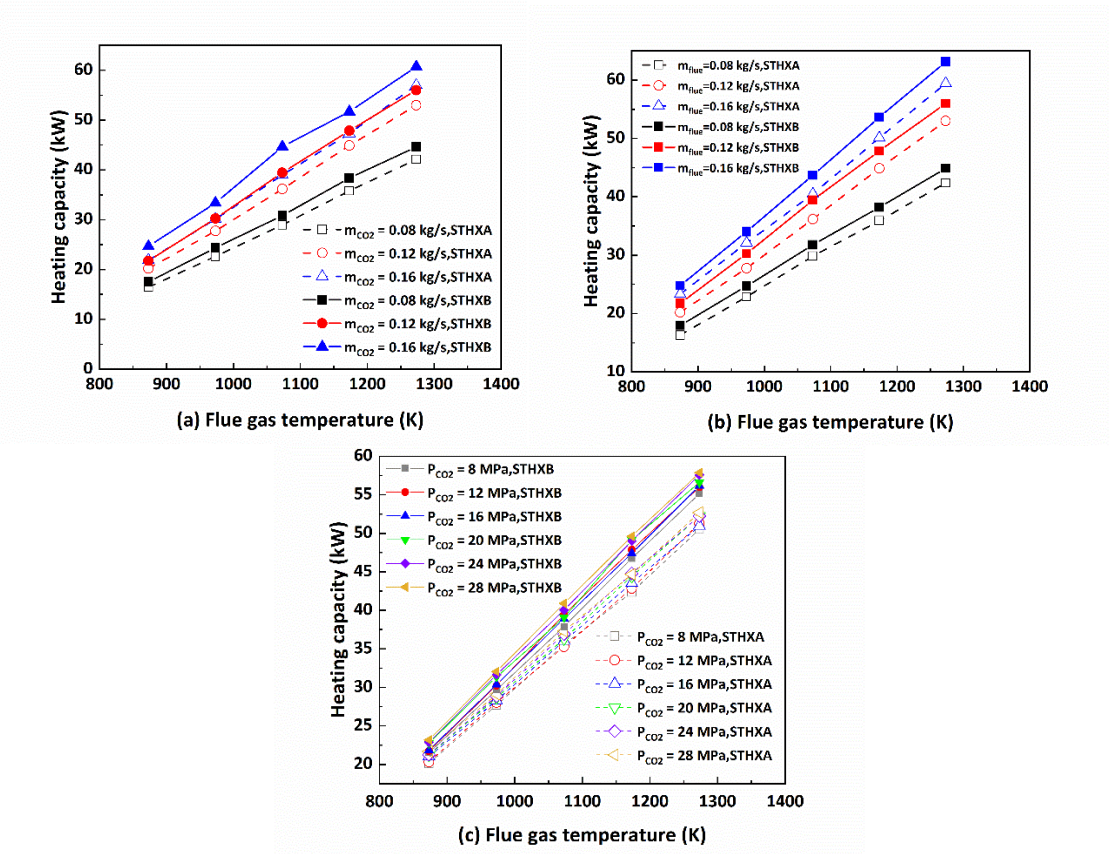

Fig. 15. Comparisons of heating capacity for STHXA and STHXB.

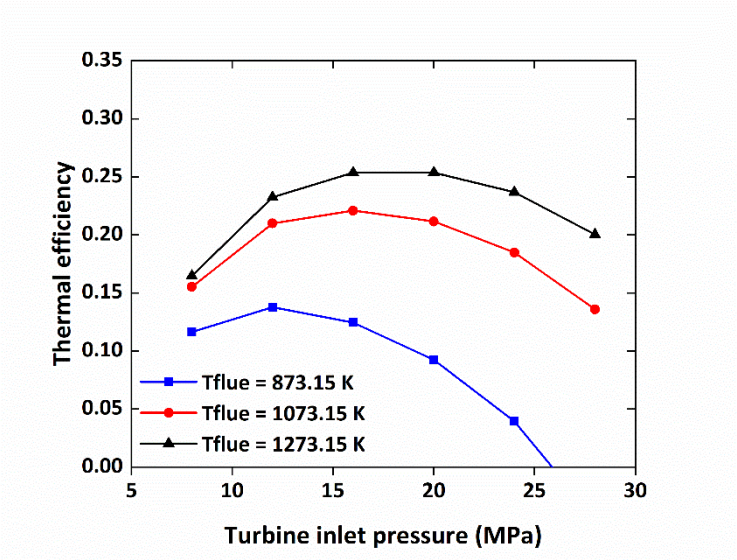

Fig.16. Thermal efficiency of STHXA at different flue gas temperature and turbine inlet pressure.

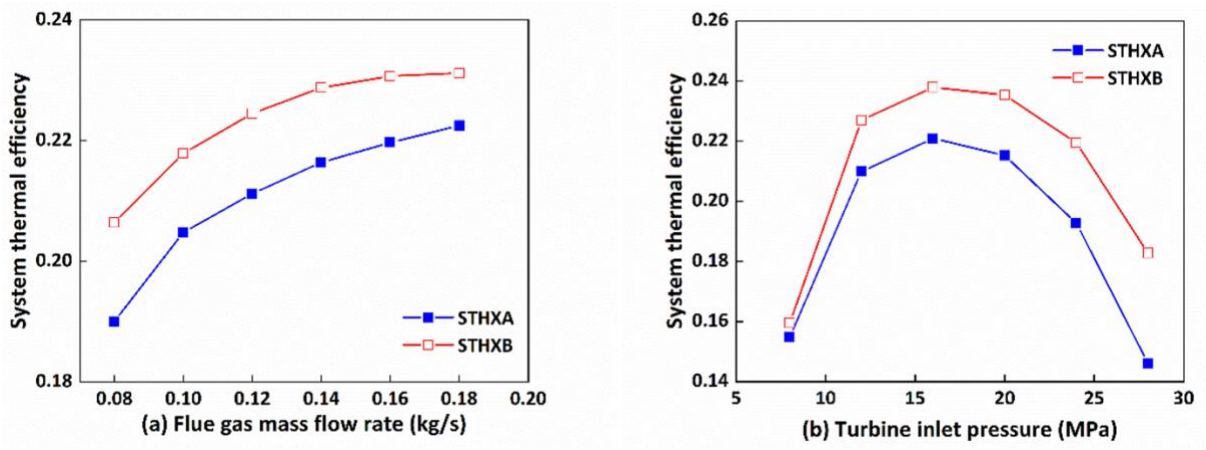

Fig. 17. comparisons of thermal efficiency for STHXA and STHXB.

Table 1

Specifications of STHX.

Name	Dimensions (mm)
Length of shell	3472
Number of inner tubes	13
Inner tube diameter	13.7
Inner tube thickness	2.24
Shell tube diameter	101.60
Shell tube thickness	3.05
Number of tube-side passes	1
Baffle distance	1157
Distance between flue gas inlet and outlet	2578

Table 2

Simulated operating conditions.

Biomass flue gas		Carbon dioxide		
Temperature (K)	Mass flow rate (kg/s)	Temperature (K)	Mass flow rate (kg/s)	Pressure (MPa)
873.15~1273.15	0.08~0.16	495~745	0.08~0.16	8~28
1073.15(design)	0.12(design)	595(design)	0.1272(design)	12 (design)

Table 3

Coefficients of c_1 ~ c_6 in Eq.(21).

$\dot{m}_{flue}$ (kg/s)	c_1	c_2	c_3	c_4	c_5	c_6
0.08	1.08E-05	0.3082086	0.000782	0.000280851	0.005645	0.434771
0.1	1.08E-05	0.2572843	0.000672	0.000280843	0.003945	0.434724
0.12	1.05E-05	0.2092301	0.00057	0.000280859	0.002981	0.434587
0.14	1.07E-05	0.2041829	0.000465	0.00028084	0.002293	0.434733
0.16	1.06E-05	0.1922788	0.00038	0.00028084	0.001845	0.434744
0.18	1.06E-05	0.193391	0.00034	0.000280841	0.001476	0.434754
0.2	1.08E-05	0.2700277	0.000667	0.00028084	0.000798	0.434758

Table 4

Coefficients of c_1 ~ c_6 in Eq.(22).

P_{co2} (MPa)	c_1	c_2	c_3	c_4	c_5	c_6
8	0.00034418	0.01435	3.51E-05	0.036705	0.000435	0
12	0.00034594	0.024892	3.51E-05	0.036361	0.000431	0
16	0.00034594	0.024892	3.51E-05	0.036361	0.000431	0
20	0	0.117314	0.000286	0.03598	0.000358	0
24	0.00013974	0.067759	0.000151	0.036271	0.000414	1.81E-08
28	8.4241E-08	0.091059	0.000289	0.035994	0.00037	1.81E-08